Piston Bowl Geometry Effects on Combustion Development in a high-speed light-duty Diesel Engine

Federico Perini, Wisconsin Engine Research Consultants, LLC
Stephen Busch, Sandia National Laboratories
Kan Zha, Sandia National Laboratories
Rolf D. Reitz, Wisconsin Engine Research Consultants, LLC
Eric Kurtz, Ford Motor Company

Abstract

In this work we studied the effects of piston bowl design on combustion in a small-bore direct-injection diesel engine. Two bowl designs were compared: a conventional, omega-shaped bowl and a stepped-lip piston bowl. Experiments were carried out in the Sandia single-cylinder optical engine facility, with a medium-load, mild-boosted operating condition featuring a pilot+main injection strategy. CFD simulations were carried out with the FRESCO platform featuring full-geometric body-fitted mesh modeling of the engine and were validated against measured in-cylinder performance as well as soot natural luminosity images. Differences in combustion development were studied using the simulation results, and sensitivities to in-cylinder flow field (swirl ratio) and injection rate parameters were also analyzed. In-cylinder mixture formation analysis showed that ignition of the pilot injection mixture develops nearly as it would in a homogeneous adiabatic reactor, being mostly advected, not mixed, by the bowl's swirling motion, while its timing is influenced by the local flow field. Details of the local in-cylinder flow are also more crucial than injection parameters in igniting the main injection's premixed fuel, as it determines the relative overlap with the high-temperature pilot ignited mixture. Bowl geometry effects drive diffusive and late-cycle combustion, as structural differences of the main injection spray flames appear due to the different impact geometries at the piston bowl rim. However, these do not affect wall heat transfer significantly: it is dominated by the piston surface area. Better air utilization with the stepped-lip geometry, thanks to greater azimuthal spreading at the rim, a strong recirculating vortex in the squish region, and better mixing in the bowl, is responsible for better late-cycle combustion efficiency and lower soot emissions.

Introduction

Diesel engines are being put under pressure by increasingly tighter requirements of lower emissions and higher fuel efficiency. Combustion chamber design, together with injector parameters and intake port design, is one of the major factors which affect the engine's fuel efficiency and pollutant emission behavior [1]. Conventional high-speed diesel engine pistons feature a re-entrant, omega-shaped bowl. In these geometries, in-cylinder flow is dominated by squish-swirl interactions near TDC [2, 3]: squish flow does work on the swirling flow to increase its angular velocity, yielding a vertical-plane flow structure, a toroidal vortex which limits fuel penetration inside the squish region volume and carries fuel-rich mixture into the bowl. The radial momentum of the spray jets can also perform work on the swirling flow by partially redistributing as additional rotational energy. This operation also introduces flow strain which will increase late-cycle turbulence production [2].

Stepped-lip bowls [4, 5] have been employed as means to improve turbulent flow structure and mixing behavior, but the mechanisms responsible for these changes are not well understood yet. Automatic genetic algorithm optimization in the work of Wickman et al. found a step-lip geometry as an optimal design which led to significant emission reductions, especially at retarded injection timing [6]. Air utilization in stepped-lip pistons may improve via a better fuel split at the step, which helps decrease soot emissions and improve indicated efficiency. Kurtz et al. suggested that improved air utilization in the squish region may be responsible for higher mixing-controlled heat-release rates [4]. Dolak et al. improved combustion efficiency by achieving two spatially separated combustion events [7]. Styron et al. found that a stepped-lip bowl produces a more even mixture distribution than a conventional bowl above the squish region [1]. Dual vortex structure resulting from optimal fuel split at the step are often identified as a means to improve air utilization [8, 9, 10].

Recent experimental and numerical studies comparing a conventional, re-entrant piston and a stepped-lip piston indicated that, for a medium-load conventional diesel combustion operating condition, benefits in mixing controlled heat release with the stepped-lip bowl are sensitive to injection timing [11], and that the reason should be sought in the step's ability to generate a well-balanced upper recirculation vortex [12]: with a conventional bowl, most fuel is always directed towards the bowl; while in a stepped-lip geometry, the amount of fuel being directed towards the squish volume varies significantly based on the injector-piston targeting, and on the flow's ability to generate an adverse pressure gradient at the step.

In this work, changes in combustion behavior due to piston geometry in a light-duty direct-injection diesel engine, equipped with two bowl designs, were studied using CFD simulations. The simulations, performed with the FRESCO platform [13], reproduced experiments carried out in the Sandia single-cylinder optical engine facility, at a medium-load, mild-boosted operating condition featuring a pilot+main injection strategy. Two piston bowl designs were used: a conventional, omega-shaped piston, and a stepped-lip piston.

Building up from previous work on in-cylinder flow, turbulence and mixing, this study aimed at understanding the causes of different combustion development with the different piston geometries, and the sensitivities of each piston geometry to operating parameters. Differences in in-cylinder flame structure were studied first, and sensitivities to in-cylinder flow field (swirl ratio) and injection rate parameters were also analyzed. A theory for the different mutual interactions of pilot and main injection pulses was established. The study of bulk mixing revealed that most soot emission reduction in the stepped-lip geometry arises from its weaker flow structures inside the bowl. Finally, a study of heat transfer suggested that, despite different flame structures at the walls, thermal efficiency benefits correlate directly with the piston surface area.

Simulation setup

The FRESCO CFD simulation platform was used for the current study. A modern Fortran toolkit, it implements an unstructured, parallel volume-of-fluid solver for the turbulent Navier Stokes equations with automatic domain decomposition for variable-topology meshes. More details about FRESCO are given in [13]. Turbulence is modeled using a generalized re-normalization group (RNG) turbulence closure model that was previously validated with engine flows, as well as for impinging and reacting jets [14]. Fuel injection and spray phenomena are modeled with an enhanced Lagrangian-Droplet/Eulerian-Fluid (LDEF) approach [15], whose model constants were optimized against Engine Combustion Network data [16]. No further tuning was performed for the current study, as comparisons with experimental liquid and fuel vapor data were in good agreement [17]. Combustion chemistry is handled by the fast SpeedCHEM chemistry solver [18, 19], which employs fully analytical sparse representation of the chemistry Jacobian, and direct solution of its associated linear systems. A dynamic adaptive chemistry method via high-dimensional clustering is employed for additional speedup at the finite-volume domain level [20, 21]. Table 1 is a summary of the combustion solver setup, while Table 2 summarizes the sub-models employed for turbulence and spray modelling. Table 3 reports values for all the spray model constants employed, same as in [15].

Table 1. Combustion models employed for the current study.

Solver	Sparse analytical Jacobian (SpeedCHEM) [19]
ODE integration	LSODES [22]
Mechanism	ERC multiChem, n_s=229, n_r=1034, Ra and Reitz [23]
DAC	High-Dimensional Clustering, ε_Y=1e-4, ε_T=10K [20]
NOx chemistry	GRI-mech 3.0, n_r=12
Soot chemistry	2-step (Hiroyasu), E_{sf} = 6290/K, A_{sf} = 700.0

Table 2. Computational model setup employed for the current study.

Phenomenon	**Sub-model**
Turbulence	Generalized re-normalization group (GRNG) k-ε [24, 14]
Injection	Blob model with dynamic blob allocation [15]
Spray angle	Reitz and Bracco [25]
Spray breakup	Hybrid KH-RT instability, Beale and Reitz [26]
Near-nozzle flow	Unsteady gas-jet model with implicit momentum coupling [15]
Drop drag	Analytical with Mach number effects [15]
Droplet collision	Deterministic impact; bounce, coalescence, reflexive separation, and stretching separation [27]; dynamic radius of influence [15]
Evaporation	1D discrete multi-component fuel [28]
Piston compressibility	Static, Perini et al. [29]

Table 3. Spray models calibration employed for the current study (same as [15]).

Parameter	Name	Value
RT breakup time constant	C_{RT}	0.10
RT breakup wavelength constant	$C_{\lambda RT}$	0.05
KH breakup decay timescale	B_1	40.6
Gas-jet assumed Stokes number	St	0.15
Gas-jet entrainment constant	K_{entr}	0.85
Max gas-jet weight near nozzle	γ_{max}	0.7
Min gas-jet weight near nozzle	γ_{min}	0.6
KH decay timescale after splash	$B_{1,s}$	1.732
KH breakup wavelength constant	$C_{\lambda KH}$	0.61
KH child birth mass fraction	f_{KHbrth}	0.03
KH child velocity factor	C_{vKH}	0.188

The Sandia optical small-bore research engine was used in this study. It is equipped with an optically-accessible piston assembly manufactured with fused silica, which retains a complete geometric representation of the piston bowl shape. The full engine geometry also included intake and exhaust surge tanks in the optical facility; intake and exhaust runners, which embed swirl plates for variable swirl ratio operation; as well as the intake and exhaust ports, cylinder, and the optical piston.

Table 4: Engine and fuel injector geometry data

Bore	82.0 mm
Stroke	90.4 mm
Connecting rod length	166.7 mm
Squish height	1.36 mm
Geometric compression ratio	15.8 : 1
Injector nozzle holes × diameter	7 × 139 µm
Nozzle hole conicity (k_s)	1.5
Injector included angle	149°

Table 5: Engine operating point and simulation boundary conditions. Note the naming convention for the two injection timings.

<table>
<tr><td>Engine speed</td><td colspan="3">1500 rpm</td></tr>
<tr><td>Intake pressure</td><td colspan="3">151 kPa</td></tr>
<tr><td>Intake temperature</td><td colspan="3">353 K</td></tr>
<tr><td>Coolant temperature</td><td colspan="3">363 K</td></tr>
<tr><td>Exhaust pressure</td><td colspan="3">145.7 kPa (constant)</td></tr>
<tr><td>Intake charge composition</td><td colspan="3">79.2 vol% N_2
19.7 vol% O_2
1.1 vol% CO_2</td></tr>
<tr><td>Swirl ratio (Ricardo)</td><td colspan="3">2.2 (both intake swirl plates open)</td></tr>
<tr><td>Fuel</td><td colspan="3">DPRF58</td></tr>
<tr><td>Injection pressure (baseline)</td><td colspan="3">800 bar</td></tr>
<tr><td>Pilot-main hydraulic dwell</td><td colspan="3">11.5 CAD</td></tr>
<tr><td rowspan="3">Injection timing</td><td></td><td>Near-TDC (SSE17)</td><td>Intermediate (SSE07)</td></tr>
<tr><td>Pilot SSE (degs aTDC)</td><td>-17.0</td><td>-7.0</td></tr>
<tr><td>Main SOI (degs aTDC)</td><td>-0.9</td><td>9.1</td></tr>
</table>

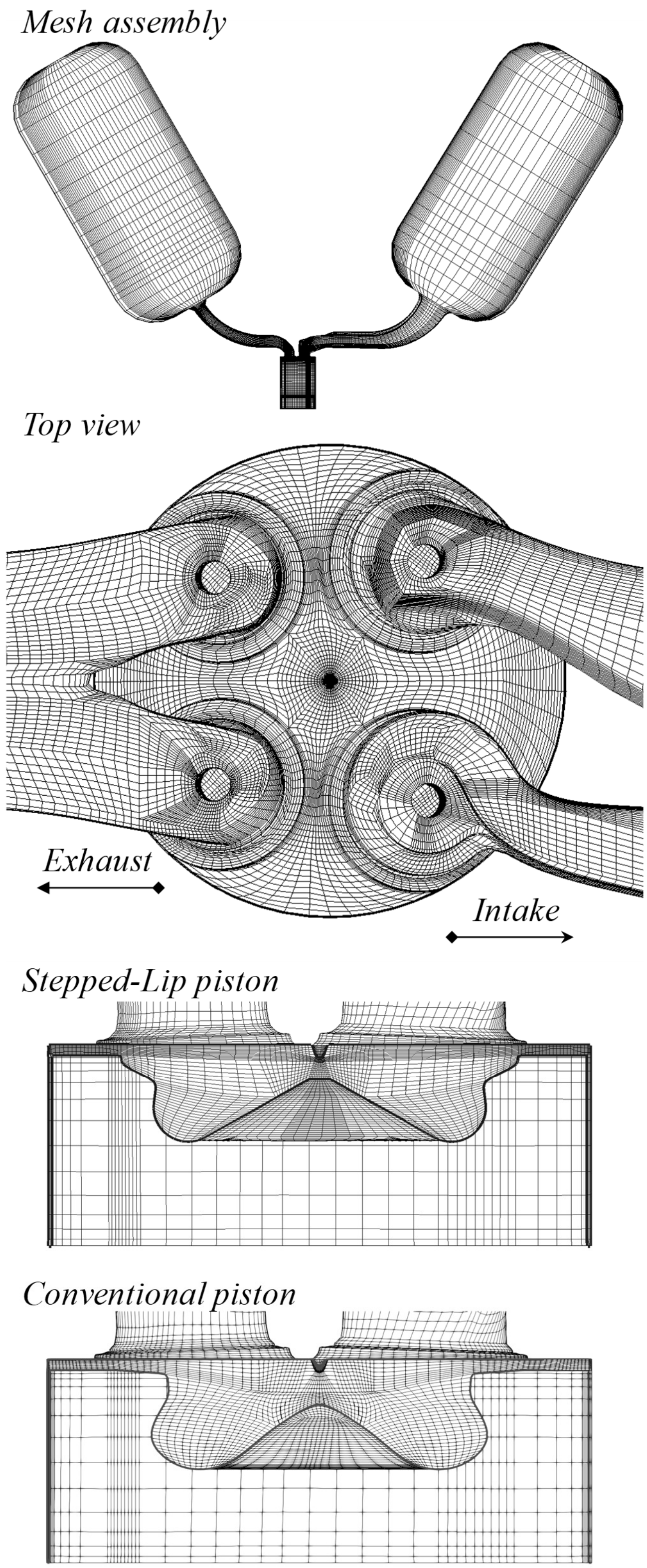

Figure 1. Full-engine CFD mesh used in this study. Cutaway views are shown to depict each piston bowl. The large intake and exhaust plenums represent the single-cylinder research engine setup.

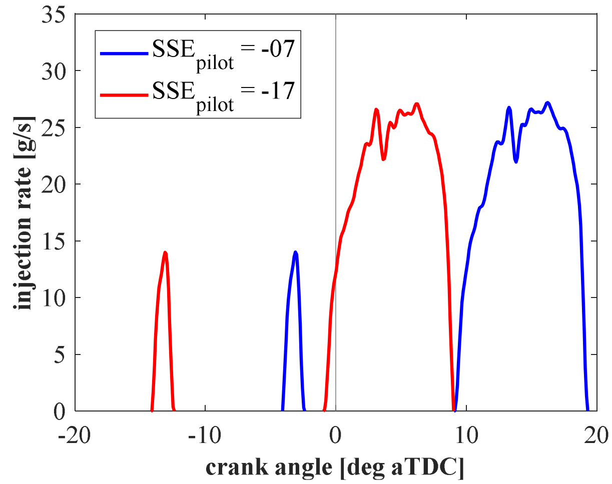

Figure 2. Simulated injection rate profiles for the two injection strategies [30].

Engine geometric data is summarized in Table 2, as available on the ECN website [31]. An unstructured, body-fitted, hexahedral mesh, with 725k cells at bottom dead center, was used for the full engine model [32], for optimal boundary layer modelling, as represented in Figure 1. Details of the 7-hole injector used in this study are also given in Table 4. The simulations matched actual spray targeting used in the engine experiments: adjusted injector tip protrusion values were used for each piston, in order to guarantee optimal near-TDC injector-piston targeting. Targeting data is available on the ECN website, as well as measured injection rate laws for the baseline cases [30].

Two consecutive cold-flow cycles were simulated to reach acceptable convergence of the flow field prediction at IVC, while keeping the total computational time reasonable, according to the methodology reported in [3]: each simulation being initialized at the time of exhaust valve opening of cycle 0, where a synthetic swirling flow field initialization corresponding to a small residual swirl level (Rs = 0.05) is imposed. Turbulence levels, density, pressure, temperature, and composition are initialized as homogenous for each of three regions: (1) cylinder; (2) intake ports, runners, and surge tank; (3) the exhaust ports, runners, and surge tank. Cycle 1 is simulated in its entirety but without fuel injection. Results of previous investigations indicate that after this cycle, the most significant features of in-cylinder flow are well converged [3]. The in-cylinder flow field at IVC of cycle 2 from the cold-flow simulation is directly mapped as an initial condition to the combusting simulation. Region-averaged values for turbulence quantities (turbulence intensity and length scale) and thermodynamic quantities (temperature and pressure fields) are also mapped to the combusting calculation, as homogeneous initial field values. Validated in-cylinder flow field and equivalence ratio predictions can be found in [33].

Engine operating conditions for the current study are given in Table 3 and represent corresponding experimental conditions [34]. A same operating point representing a part-load (9bar IMEP), conventional diesel combustion strategy (CDC9) with a split pilot-main injection strategy was employed. Injection takes place in a slightly-dilute, reacting environment with 19.7 vol% oxygen content. Two injection schedules were employed, where the pilot-main dwell is constant, and the injection rate law is block shifted. They are identified by start of solenoid energizing (SSE) timing for the pilot injection: a SSE=-17 deg aTDC, or “near-TDC” main injection, has a main injection pulse starting shortly before top dead center; SSE=-7 deg aTDC, or “intermediate” injection timing, leads to efficiency and emissions advantages over the conventional piston when fired thanks to faster mixing-controlled heat release, and the main injection pulse starts at approximately 9.1 CA deg aTDC [11]. Baseline injection rate profiles were measured with a hydraulic injection rate meter [30], and are represented in Figure 2.

Results and discussion

Validation

In-cylinder pressure and heat release rate profile validation for both injection timings is reported in Figures 3, 4 for the conventional piston and Figures 5, 6 for the stepped-lip piston. The CFD simulations behaved consistently across all simulated results, as the same spray setup, and no additional calibration (i.e. of the injection rate timings) were introduced to avoid adding further uncertainty to the interpretation of the results. In all cases, pilot and main injection ignition delay times (IDT) were well-predicted using the multiChem mechanism, despite shock tube data for a detailed kinetics validation with the large alkanes in DPRF fuels not being available yet. The largest discrepancy in heat release (HR) rates was seen for the premixed HR peak at the beginning of the main injection for the SSE17 case. As Figure 7 shows, this is the location where the largest cycle-to-cycle variability is seen in the experiments. With the stepped-lip piston, a slightly under-predicted diffusive heat release rate plateau was predicted. Also, different late-cycle heat release profiles with injection timing were correctly captured for both pistons: exponential-decay-like for the SSE07 strategy, and with an elbow at ~15 degrees aTDC for the SSE17 strategy.

Soot natural luminosity. In-cylinder predictions were also compared against in-cylinder soot natural luminosity (NL) images ***[34]*** for additional validation of the local flow and flame structures. For this study, the same soot model constants suggested by Hessel et al. ***[35]*** for the 2-step Hiroyasu model were employed (Table 2). The study of ***[35]*** showed that it is possible to achieve quantitative comparisons of CFD predictions with soot NL via appropriate radiative transfer functions; that requires expensive post-processing and was beyond the scope of this work. Instead, a simpler approach using volume fraction iso-surfaces was used.

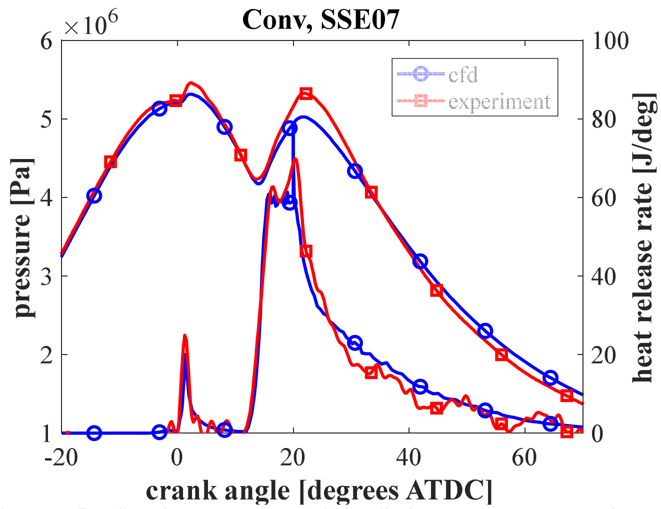

Figure 3. Predicted vs. experimental in-cylinder pressure trace and heat release rate, Conventional bowl, SSE07 injection strategy.

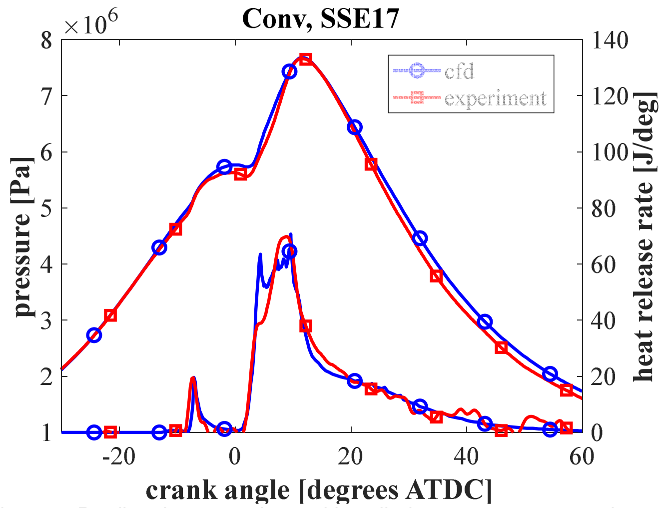

Figure 4. Predicted vs. experimental in-cylinder pressure trace and heat release rate, Conventional bowl, SSE17 injection strategy.

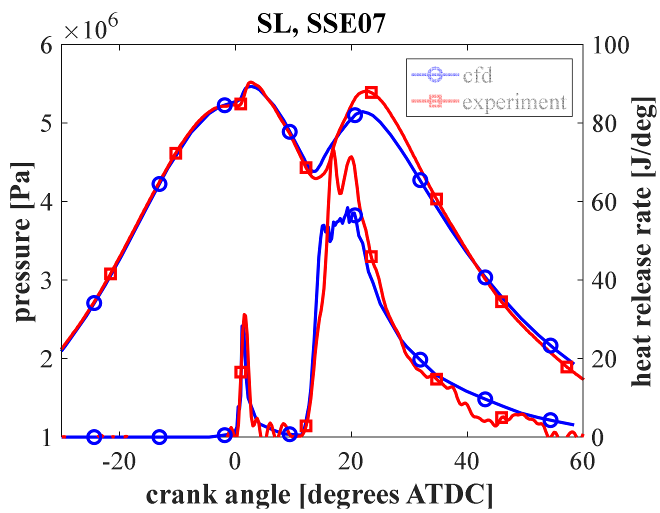

Figure 5. Predicted vs. experimental in-cylinder pressure trace and heat release rate, Stepped-lip bowl, SSE07 injection strategy.

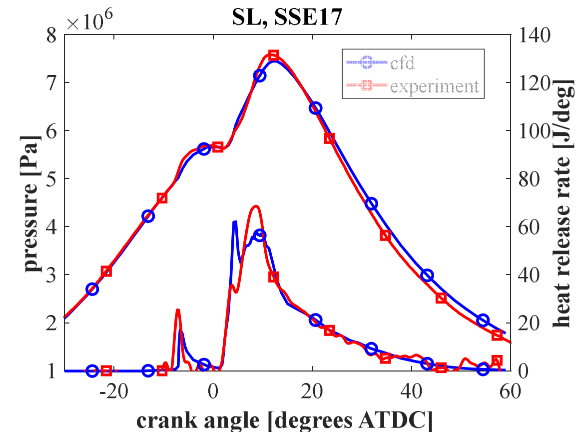

Figure 6. Predicted vs. experimental in-cylinder pressure trace and heat release rate, Stepped-lip bowl, SSE17 injection strategy.

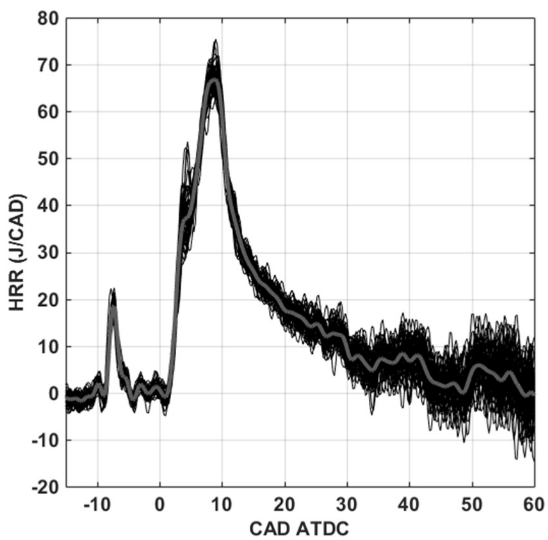

Figure 7. Measured heat release rate traces for 50 individual cycles (black) and ensemble-average (red) for the Conventional piston, SSE17 case.

For each of the images in Figures 8,9,10, five soot volume fraction isosurfaces were drawn at predicted soot levels fv = [1, 5, 10, 15, 20] ppm; each of these surfaces is semi-transparent and contoured by temperature. When overlapping, these isosurfaces yield a thicker, less transparent plot, which mimics the effects of a larger transfer function integral along the line of sight.

The soot ensemble-averaged NL images indicated drastically different soot formation/oxidation patterns inside the bowl and in the inner squish region (near-bore radii and the step lip regions are experimentally invisible). In both pistons, little to no soot is seen forming during the pilot injections, so the images begin with the main injection. In Figure 8, early soot formation appears as the main injection hits the piston bowl surface, where rich high-temperature pockets stagnate and are then advected outward to the squish and deep into the bowl. The stagnation points, counterclockwise tilted due to swirling motion, represent the soot NL peak at this stage.

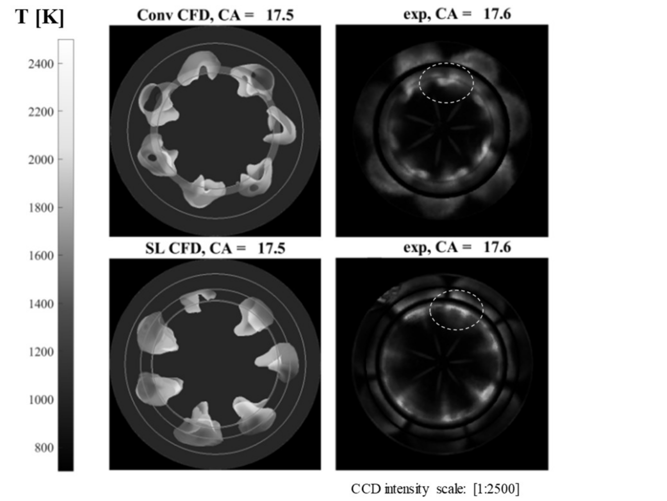

Figure 8. Measured (right) ensemble-averaged soot natural luminosity vs. predicted soot concentration (fV = [1,5,10,15,20] ppm) contoured by temperature. SSE07 case, CA=17.5 aTDC, top: conventional piston; bottom: stepped-lip piston. Regions of early soot formation highlighted in yellow.

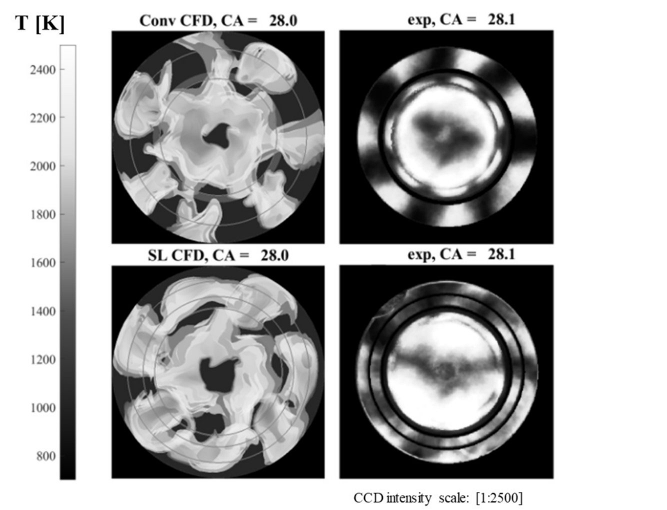

Figure 9. Measured (right) ensemble-averaged soot natural luminosity vs. predicted soot concentration (fV = [1,5,10,15,20] ppm) contoured by temperature. SSE07 case, CA=28.0 aTDC, top: conventional piston; bottom: stepped-lip piston.

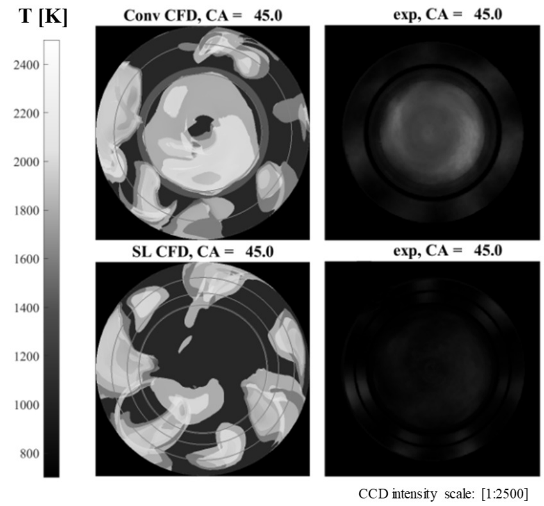

Figure 10. Measured (right) ensemble-averaged soot natural luminosity vs. predicted soot concentration (fV = [1,5,10,15,20] ppm) contoured by temperature. SSE07 case, CA=45.0 aTDC, top: conventional piston; bottom: stepped-lip piston.

In Figure 9, a later stage is shown, after all fuel from the main pulse has been injected. The model shows that most soot is now located inside the bowl, and the soot cloud is more organized into an annular structure in the conventional piston. The model also shows significant amounts of soot reach the squish volume near the cylinder liner, beyond the field of view of the experimental imagery. In the stepped-lip geometry, the squish soot cloud exhibits larger azimuthal extent, as the fuel vapor jets also merge azimuthally, while separate jets are still seen with the conventional bowl. Figure 10 represents late-cycle soot structure. Soot NL intensity is lower and the fv isosurfaces have smaller spatial extent, as most soot from the main injection has already been oxidized. At this stage, significant discrepancies arise: with the conventional piston, much more residual soot is present inside the bowl than with the stepped-lip one. The residual soot cloud still resembles the toroidal structure originating in Figure 9, even 18 crank angle degrees later.

Despite the relatively simple model, the local soot NL analysis showed acceptably good agreement of the simulation also in terms of local in-cylinder quantities.

Combustion development analysis

Combustion phenomenology was analyzed looking at in-cylinder flame structures. Diesel flames were reproduced using volume rendering of temperature with a threshold $T_{flame} \geq$ 1500K; liquid fuel structure was represented by the computational parcels, sized by parcel volume and contoured by liquid-phase temperature. Figure 11 represents combustion development in both piston geometries for the SSE07 case.

<u>Pilot injection</u>. Pilot injection jets were seen igniting approximately 6 crank angle degrees after SOI_{pilot} (Figure 11 a)), as high-temperature pockets appear at the spray jet tips, where mixing has already occurred. With the conventional bowl, all pockets ignited almost simultaneously, while a slightly larger IDT range of approximately 3 crank angle degrees was seen with the stepped-lip geometry, where all pilot jets were ignited by 5 deg aTDC (Figure 11 b)).

With the conventional piston, greater swirl ratio is present inside the bowl, which explains the wider azimuthal stretch of the pilot-ignited pockets in Figure 11b. With greater azimuthal spreading, the high-temperature pockets in the conventional bowl make up for a larger *firewall*, which can foster ignitability of the main injection. Residual liquid-phase fuel is still present in both piston geometries, mostly located at the cylinder center, still close to the injector.

In order to have a quantitative outlook at why the pilot injections exhibited a different behavior, a stoichiometric isosurface-based reconstruction method was used. A reactive equivalence ratio field based on Mueller et al.'s atom-based formulation was computed [36]:

$$\phi = \frac{2[C]+\frac{1}{2}[H]}{[O]},$$

and a stoichiometric level-set isosurface triangulation was extracted at ϕ=1 based on the marching cells algorithm of [37]. Figure 12 highlights the piston geometry effects on relevant properties of the stoichiometric isosurface in the pilot injection's ignition delay time range (SSE07 case). The stoichiometric isosurface area has comparatively similar size, but it exhibits different behavior: with a conventional bowl, the initially formed stoichiometric pocket increases size since it is stretched by high bulk swirl, and the area starts decaying as ignition takes place. With the stepped-lip geometry, the area keeps decaying since very early after SOI_{pilot}, as a result of greater local mixing. This is confirmed by the turbulent mass diffusion coefficient:

$$D_t = \frac{\mu_t}{\rho\, Sc_t}\left[\frac{cm^2}{s}\right],$$

where μ_t is a local turbulence viscosity predicted by the GRNG k-epsilon model, ρ the local gas-phase density, and Sc_t = 0.68 a turbulent Schmidt number assumed constant and homogeneous through the domain. Assuming similar ambient density, D_t correlates linearly with the local turbulence viscosity at the stoichiometric isosurface.

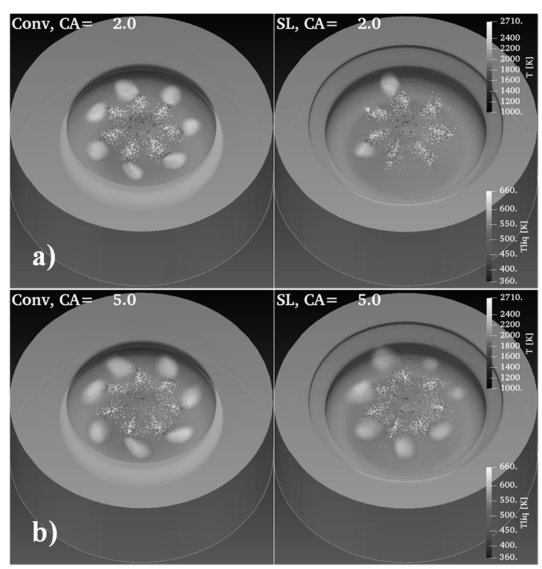

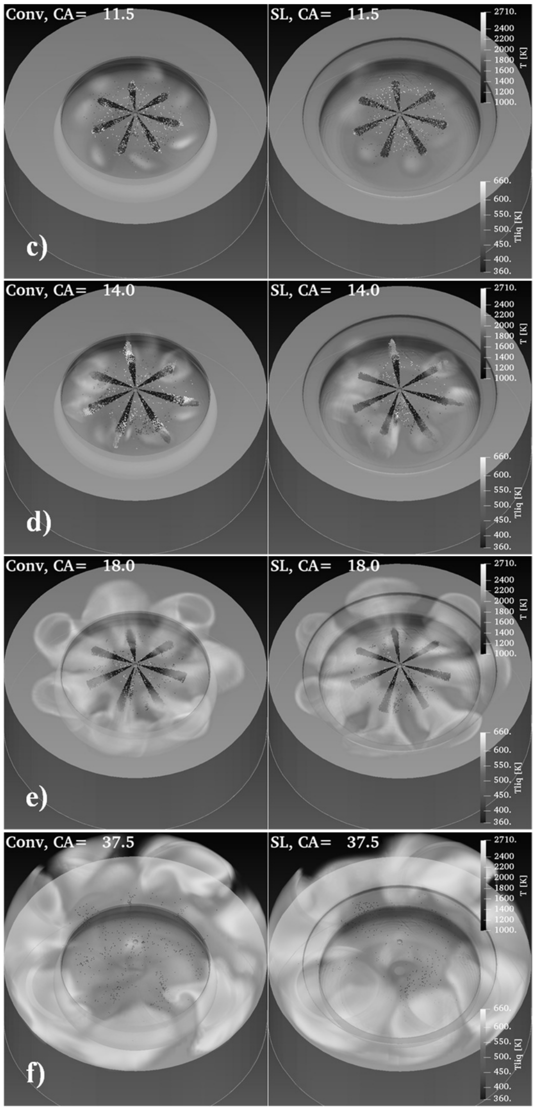

Figure 11. Combustion development for the SSE07 case. Piston geometries: (left) conventional, (right) stepped-lip. a) pilot injection ignition; b) pilot injection transport; c) early main injection; d) main injection ignition; e) main injection impact; f) late-cycle structure.

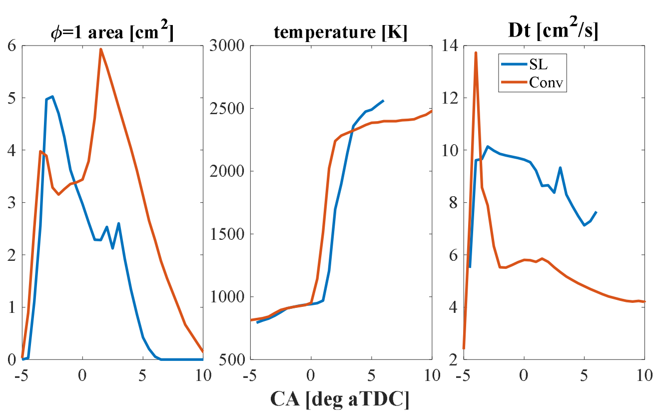

Figure 12. Piston geometry effects on ϕ=1 surface properties during pilot ignition delay time for the SSE07 case. (left) stoichiometric isosurface area; (center) surface-averaged temperature; (right) surface-averaged turbulent mass diffusion coefficient.

With the stepped-lip geometry, local mass diffusion at the turbulence scale of the pilot's stoichiometric pockets is an average 49.9% greater than for the conventional geometry (Figure 12). As a result, the pilot jets temperature in the stepped-lip geometry on average undergoes a slightly longer dwell between low- and high-temperature chemistry stages, as well as a slightly slower high-temperature heat release phase (Figure 12, center). Despite this discrepancy, both piston geometries exhibit a pretty clear homogeneous reactor-like temperature history, with well-defined low- and high-temperature stages. This suggests that the pilot injection pockets which have formed inside the bowl are *shaken, not stirred* with the surrounding flow patterns.

Main injection. Developed liquid columns due to the main injection are represented in Figure 11c. At this stage, residual fuel from the pilot injection was almost completely vaporized, and the main injection's radial penetration length was very close to the pilot injected fuel's ignited location. This would actively feed fuel vapor into the high-temperature swirling pockets from the pilot injection.

This configuration would lead to selective ignition of the main fuel jets as long as they would intersect with a high-temperature pilot ignited mixture region (Figure 11d). For the intersecting jets, fuel has ignited and diffusion flames have already started to surround them, while no high-temperature ignition was seen yet for those jets, such as the 12 o'clock jet, which reached the bowl rim in the low-temperature region between two pilot ignited pockets. This suggested that relative pilot-main clocking, affected by local flow features and injector operation, could be responsible for the high cyclic variability of premixed HR, as observed in Figure 7. Additional analysis is reported in the following section.

Fully developed Diesel flames from the main injection were seen to form as soon as the ignited main jets reached the piston bowl rims, as represented in Figure 11e. In both cases, jet split given by the impact geometry against the step determined the relative penetration both into the squish and the bowl volumes. Some jet-to-jet deviations were present, but they led to no significant differences in jet structure. With the stepped-lip geometry, high-temperature pockets past the rim had larger azimuthal extent, as the step seemed to create a wider stagnation region, which fostered greater azimuthal dispersion of the fuel; while in the central part of the cylinder, the jets merged less with one another than with the conventional combustion chamber.

Late-cycle flame structure, after the end of the main injection, is represented in Figure 11f. Developed flames are present both in the squish and the bowl volumes regardless of piston bowl geometry. Inside the bowl, the jets have merged into an azimuthally coherent

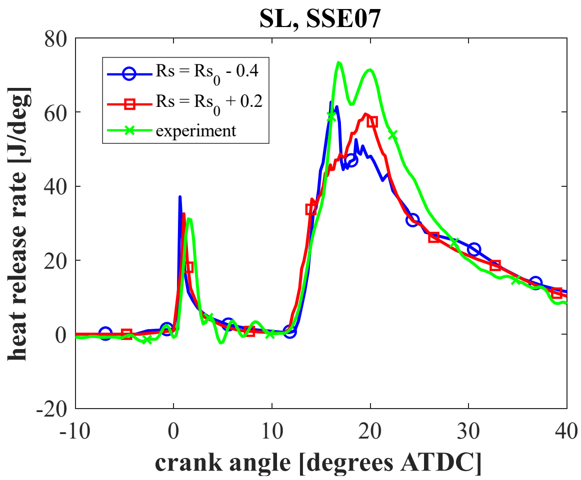

Figure 13. Swirl ratio effect on in-cylinder heat release rate. Stepped-lip piston, SSE07 injection strategy.

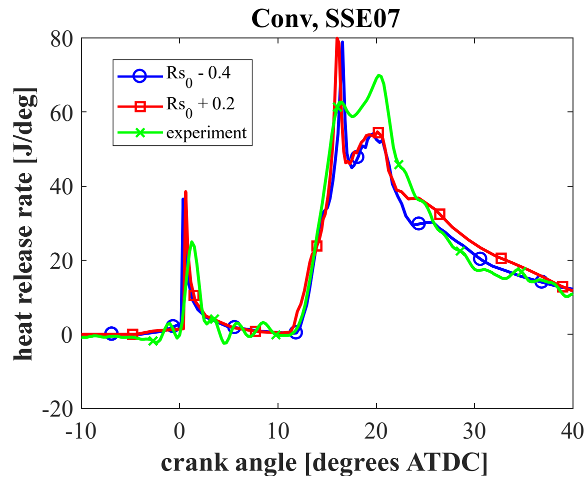

Figure 15. Swirl ratio effect on in-cylinder heat release rate. Conventional piston, SSE07 injection strategy.

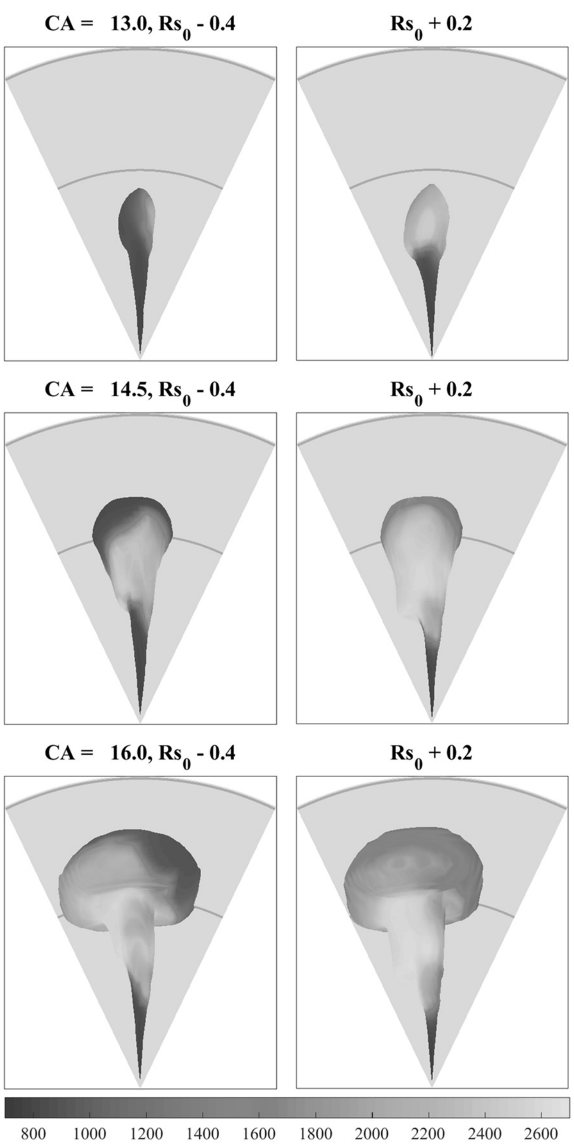

Figure 14. Swirl ratio effect on main injection ignition, stepped-lip piston, SSE07: temperature contours over ϕ=1 level set.

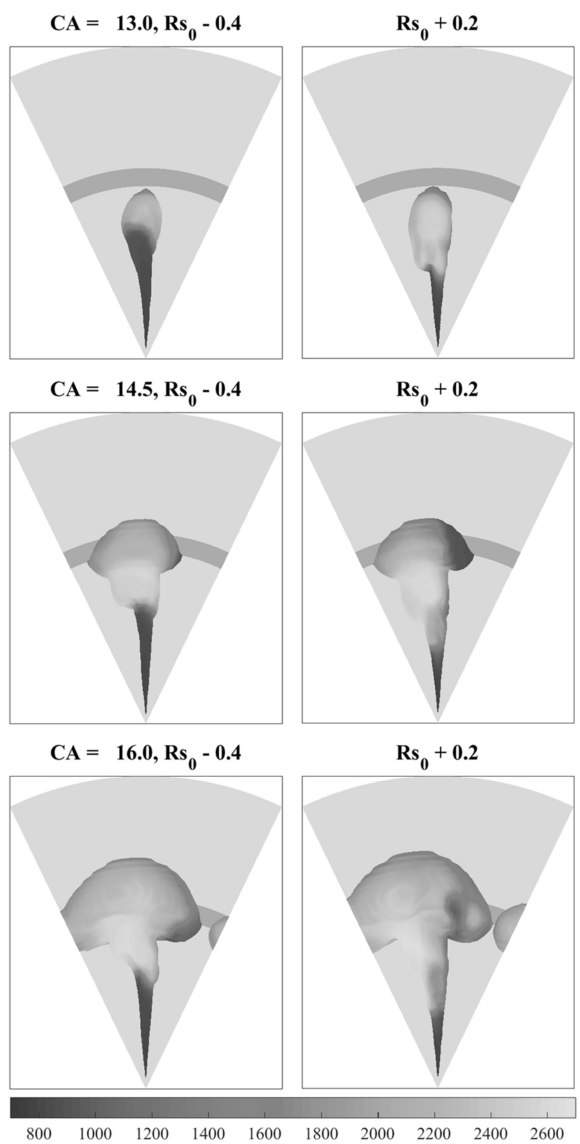

Figure 16. Swirl ratio effect on main injection ignition, conventional piston, SSE07: temperature contours over ϕ=1 level set.

toroidal structure, due to the swirling flow. Squish flames are characterized by different azimuthal extent: it is larger for the stepped-lip piston, while individual jets are still visible for the conventional bowl. Near the cylinder head, the latter are also somewhat more pushed towards the liner, while the stepped-lip jets show stronger inward flow, recirculating more towards the jet entrainment region.

Swirl Ratio and Rail Pressure Effect on Premixed HR

In order to understand the role of operating parameters on the main injection's premixed HR phase behavior of Figure 7, two sets of combusting simulations in a sector mesh model were setup: the first one focused on swirl ratio inside the bowl; the second on the initial injection momentum/mixing transient, by changing injection rate shapes according to different injector rail pressures.

Swirl ratio effect. The effect of IVC swirl ratio on the heat release traces is reported in Figures 13 and 15. In both pistons, a reference case had the same mapped IVC quantities from the full mesh simulation according to the procedure outlined in [33]; a low-swirl case had $Rs_{IVC}=Rs_0-0.4$, and a high-swirl case had $Rs_{IVC}=Rs_0+0.2$, as represented in Figure 17. In both piston geometries, the pilot injection "pockets" had different rotational speed, as suggested by the different clocking of the high-temperature regions in Figures 14,16. However, pilot ignition delay time was not significantly affected by bulk swirl. This strengthened the hypothesis that pilot injection pockets are advected, but not significantly mixed, with the surrounding flow.

Both pistons' premixed HR traces were affected by swirl, but the stepped-lip geometry exhibited the greatest sensitivity. For the stepped-lip piston (Figure 14), premixed HR is defined by the extent of the overlap between the high-temperature pockets from the pilot injection and the main injection jet. With higher swirl, better overlap is achieved, and the high-temperature pockets fosters early ignition of the main jet, which ultimately leads to a smoother premixed HR profile. With lower swirl, the pilot injection pocket overlapped with the jet only when a significant amount of fuel from the main had already reached the bowl rim. Hence, greater fuel mass would experience premixed ignition, causing a higher HR peak.

With the conventional piston, limited sensitivity to swirl ratio was predicted. As shown in Figure 16, the main injection's premixed HR peak occurs when the main spray jet reaches the thick bowl rim quickly after overlapping with the pilot. At the rim, a rich stagnation region drives the greater HR peak. Some differences arise late-cycle, as higher swirl allows for higher heat release rate because of the faster dissipation of the in-bowl toroidal vortex.

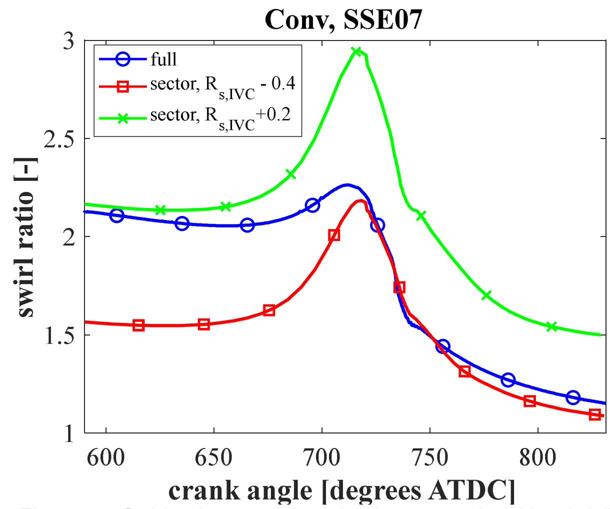

Figure 17. Swirl ratio comparison for the conventional bowl: full vs. sector mesh simulations.

Rail pressure effect. Considering that oscillations in rail pressure can be significant, an injection rate analysis was established to understand the role of the injector opening transient during the main injection pulse. A simple phenomenological model of the Bosch CRIP2.2 injector was employed [38]. Four injection pressures of 800, 1000, 1200, and 1300 bar were tested. In Figure 18, predicted injection rates for the main pulse are compared with the experimental main pulse trace, which was obtained at p_{rail} = *1200 bar* operation.

Predicted heat release traces for the stepped-lip piston are reported in Figure 19. The relative clocking between the high-temperature pilot pocket and the main jet was unaffected by rail pressure, as represented in Figure 20, and limited effect of rail pressure on the initial HR profile were seen for $p_{rail} \geq 1000$ bar. Most differences appeared later, as sustained momentum from the injection changes

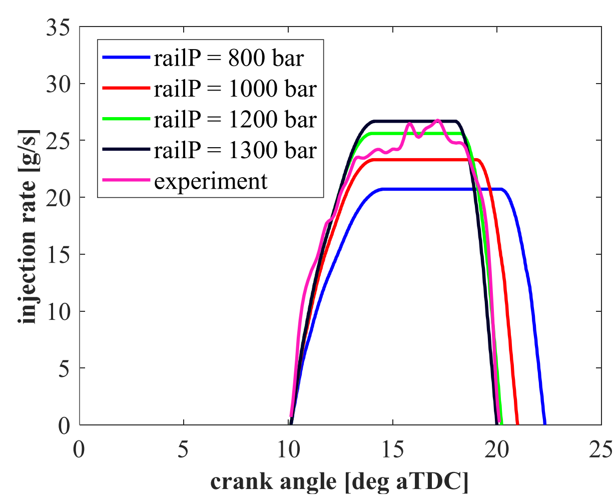

Figure 18. Main pulse injection rate profiles employed for the main injection rate / rail pressure effect study.

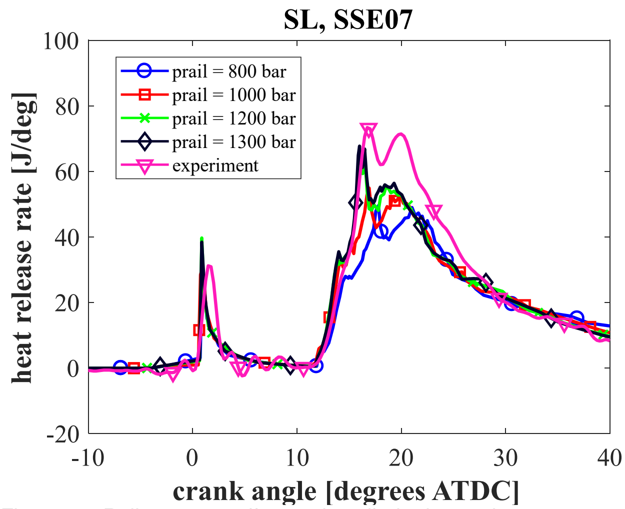

Figure 19. Rail pressure effect on in-cylinder heat release rate. Stepped-lip piston, SSE07 injection strategy.

the fuel split between the squish and bowl region. Differences after the end of injection were negligible. This suggested that the turbulent mixing conditions which prepare premixed HR in the stepped-lip geometry with a pilot-main strategy are more strongly correlated with the relative clocking caused by the pilot-main dwell and bulk swirl motion inside the bowl.

Conventional piston heat release traces at varying rail pressures are reported in Figure 21. Rail pressure effect is more pronounced than with a stepped-lip piston, as the extent and timing of the heat release peak is strongly coupled with the injection rate law. As shown in Figure 22, at higher rail pressures, faster jets reach the bowl rim's impact region sooner, which leads to higher and earlier premixed HR peaks. Lower rail pressures cause slower transient fuel jets which also exhibit a slower HR ramp-up phase. In all cases, the relative clocking between the main jet and the high-temperature pocket from the pilot injection caused near complete overlap. This did not reduce the changes in premixed HR profiles, suggesting that the driving mechanism for premixed HR in the conventional bowl is the amount of mass stagnating at the thick bowl rim as ignition takes place, and the sustained mass flux to it from the injection's momentum.

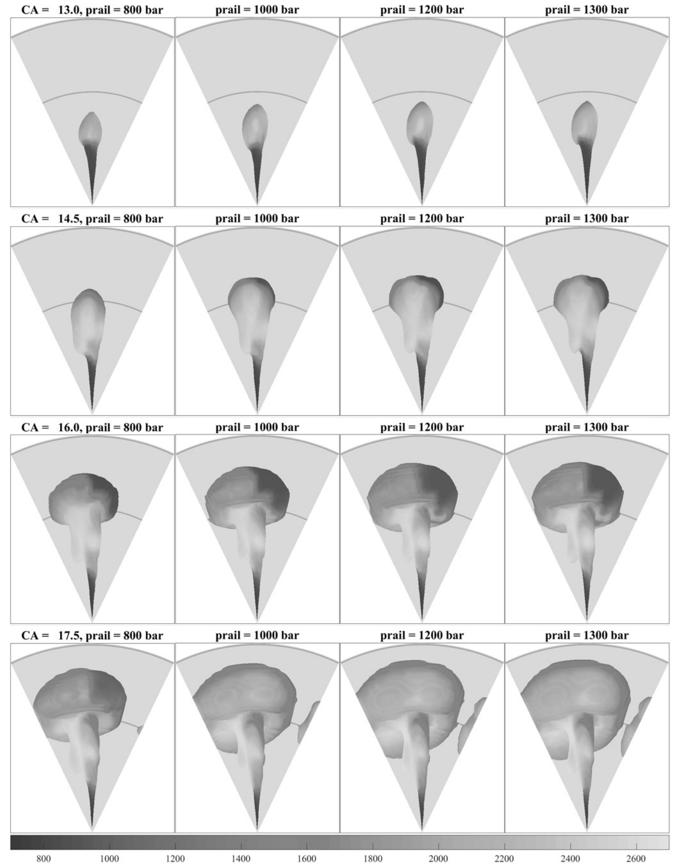

Figure 20. Rail pressure effect on main injection ignition, stepped-lip piston, SSE07: temperature contours over ϕ=1 level set.

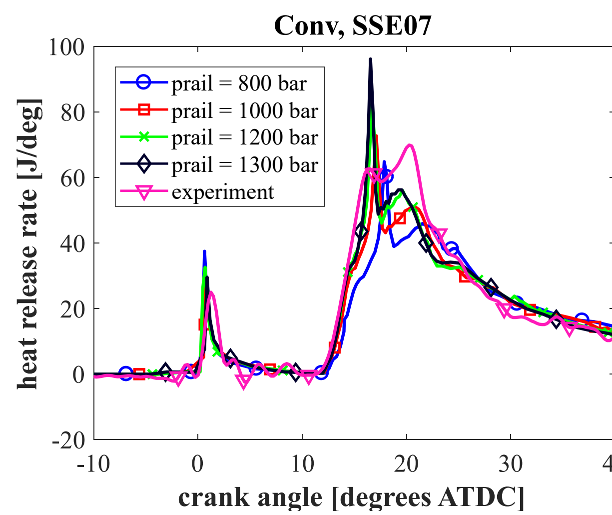

Figure 21. Rail pressure effect on in-cylinder heat release rate. Conventional piston, SSE07 injection strategy.

Convective mixing analysis

As previously observed [12], different piston geometries lead to different bulk flow patterns after the injection which may be responsible not only for different air utilization, but also for different fuel air mixing. In the attempt to understand how these could affect combustion development, we analyzed bulk mixing through air/fuel equivalence ratio isosurfaces.

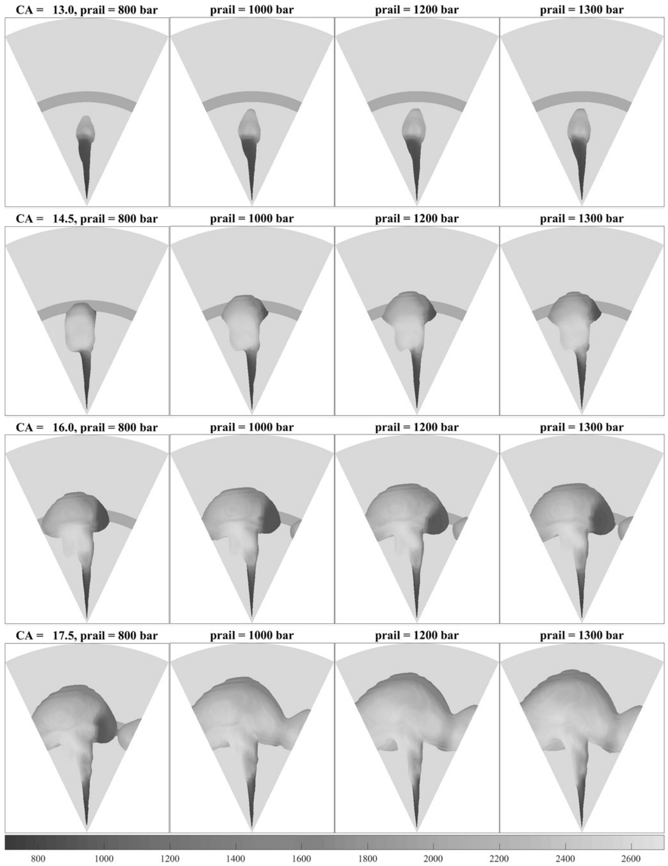

Figure 22. Rail pressure effect on main injection ignition, conventional piston, SSE07: temperature contours over ϕ=1 level set.

The reactive equivalence ratio formulation of Mueller was used to generate an in-cylinder equivalence ratio field, used to extract three iso-surfaces [37] of constant equivalence ratio: lean (ϕ=0.5), stoichiometric (ϕ=1.0) and rich (ϕ=2.0). These isosurfaces were used as a dummy, moving 'flame front' representation for the diesel flame, and local mixing was estimated as local mass flux ϕ_m through isosurface, from the moving reference frame perspective:

$$\phi_m = \int_S \rho \cdot (u_{cfd} - u_{iso}) \cdot \hat{n}\, dS.$$

In this formulation, u_{cfd} represents the interpolated CFD velocity field value at the isosurface triangulation, ρ the local mixture density and u_{iso} the local front velocity. In order to estimate the local front velocity, we employed the swept volume method of [39], where two subsequent simulation snapshots at $\Delta\theta$ = 0.5 crank angle degrees were used for the swept volume calculation. In our approach, the iso-surface normal direction points toward the low-value region, i.e., equivalence ratio normals point toward the *lean* volume. Hence, positive mass flux through an equivalence ratio isosurface indicates jet-like mixing, i.e., when fuel vapor at richer concentration meets the surrounding air driven by bulk transport. Negative mass flux instead indicates entrainment-like mixing, i.e., when fresh/leaner charge is being advected into the equivalence ratio front towards the rich region.

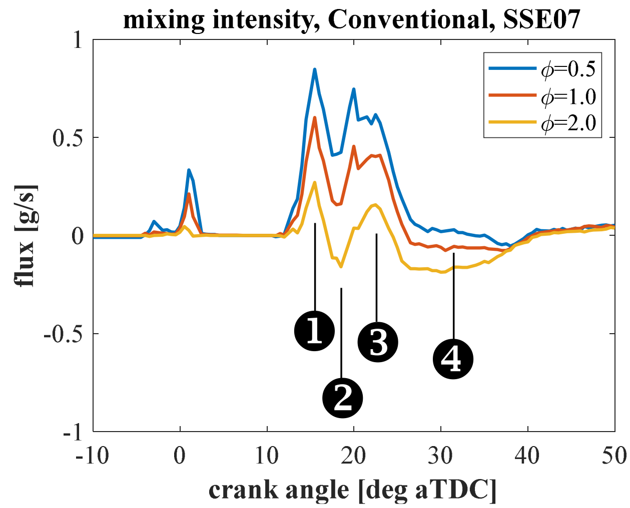

Figure 23. Mixing analysis, conventional piston, SSE07 case.

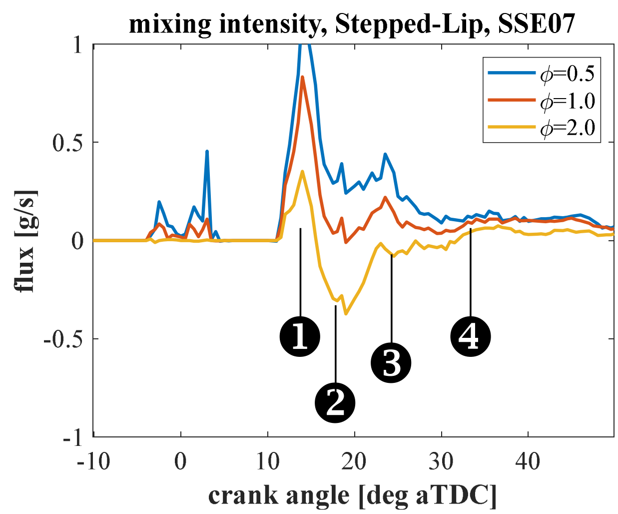

Figure 24. Mixing analysis, stepped-lip piston, SSE07 case.

Figures 23 and 24 represent in-cylinder mixing behavior for the SSE07 case at three equivalence ratio isosurfaces, while Figure 25 reports corresponding mixing iso-surface structures at relevant crank angles. Four relevant points were identified based on the observed mixing phenomenology: ❶ early main injection, at the impact with the piston bowl rim; ❷ late main injection, when established penetration into the squish and bowl volumes is present; ❸ end-of-injection behavior, shortly after the end of the main injection; ❹ late-cycle structure. The conventional piston exhibited two positive mixing peaks, early and at the end of injection, with a negative peak in between, followed by a slightly negative late-cycle behavior, towards well-balanced mixing. The stepped-lip bowl exhibited remarkably different behavior beginning with the end of injection and into the late-cycle region, as no second positive flux peak was observed.

Early into the main injection (❶), the driving mixing mechanism for both pistons is the positive flux at the piston bowl rim, caused by thermal expansion of the ignited jet, as well as fuel mass accumulation at the stagnation point. Negative entrainment flux is

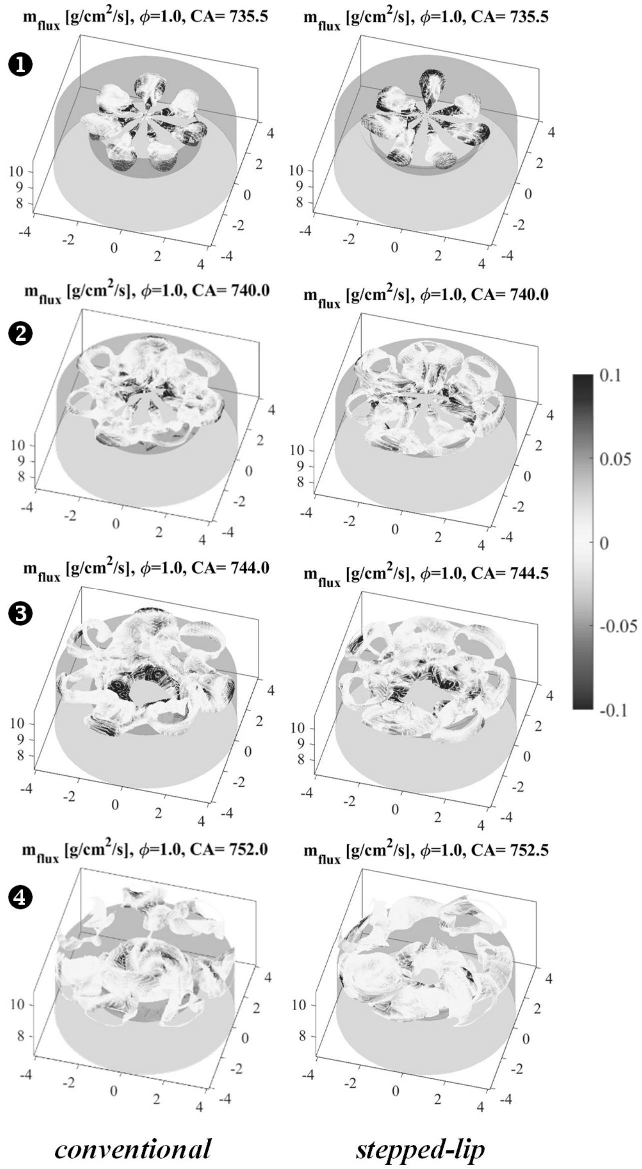

Figure 25. Mixing fluxes at the ϕ=1.0 isosurface, SSE07 case. (left) conventional piston; (right) stepped-lip piston.

present at all jets, but its area is too small to balance positive flux. As the main injection develops (❷), a drop in positive flux is seen, and on-going entrainment flux causes the global flux balance to be significantly reduced, becomingnegative for the rich ϕ=2 isosurface. The drop in positive flux appears due to reduced transport velocities at the jet tips, despite larger areas, both in the squish and the bowl penetration regions. In the stepped-lip geometry, the drop is stronger thanks to greater inward recirculation and smaller penetration velocity into the squish volume. After the end of injection (❸), positive flux is restored in the conventional geometry as penetration into the piston bowl, caused by residual momentum from the spray jets, generates additional positive mixing with the bowl's fresh charge. This mechanism is much weaker inside the stepped-lip geometry, due to both shorter penetration (less of the spray mass and momentum are directed into the stepped-lip bowl) and a shallower bowl shape. Late-cycle, the effects of this different behavior cause different mixing structures (❹): inside the stepped-lip bowl, a weak, wrinkled structure is present, its mixing being caused both by positive and negative contributions. Inside the conventional bowl, instead, a toroidal vortex has formed. Swirling motion limits mixing across this stoichiometric isosurface, whose normals are orthogonal to the main flow direction. This explains the longer persistence of a rich, sooty cloud as observed in Figure 10.

Heat transfer

An investigation on wall heat transfer was carried out to understand whether different hot temperature gas footprints on the engine's surfaces could affect the overall thermal efficiency. For each piston geometry, heat flux at three separate surfaces was analyzed: *piston* (not including the crevice region), *head* (not including the colder valve bottoms), and *liner*. For reduced mesh dependency of the heat transfer predictions, the two models have identical azimuthal resolution, and nearly identical radial discretization at the walls, employing o-grid refinement. y^+ predictions are similar in each region, as reported in Figure 26: during injection, most piston values are in the [50, 150] range, head values in the [100, 200] range and liner values in the [20, 40] range. CFD-predicted heat flux follows Han and Reitz's thermal law of the wall formulation [40]:

$$q_w = \begin{cases} \dfrac{c_p \rho u^* (T - T_{wall})}{y^+ \, \mathrm{Pr}_t}, & y^+ \leq 11.05 \\ \dfrac{c_p \rho u^* T \log(T/T_{wall})}{2.1 \log(y^+) + 2.513}, & y^+ > 11.05 \end{cases}$$

Figures 27 and 28 report surface-integral instantaneous wall heat fluxes for the SSE07 and SSE17 injection timings.

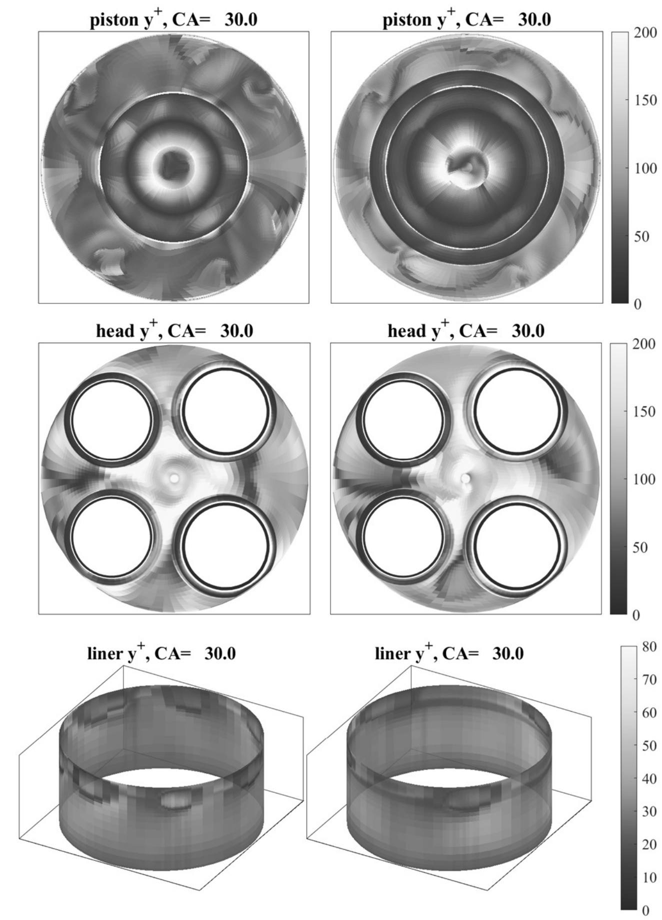

Figure 26. Predicted wall y^+, SSE07 case.

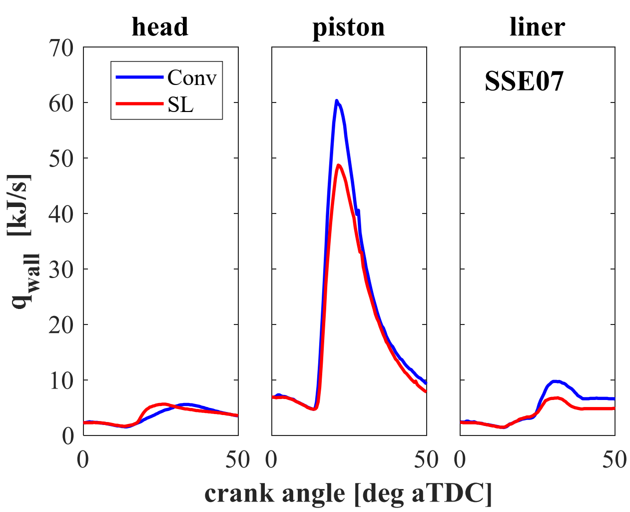

Figure 27. Instantaneous wall heat flux comparison for the SSE07 case.

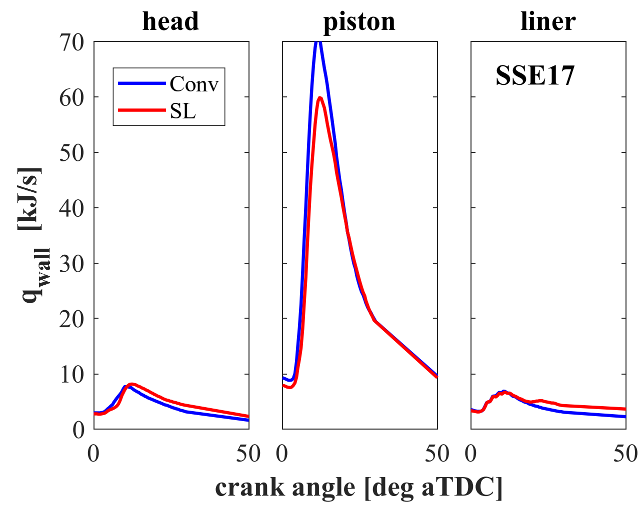

Figure 28. Instantaneous wall heat flux comparison for the SSE17 case

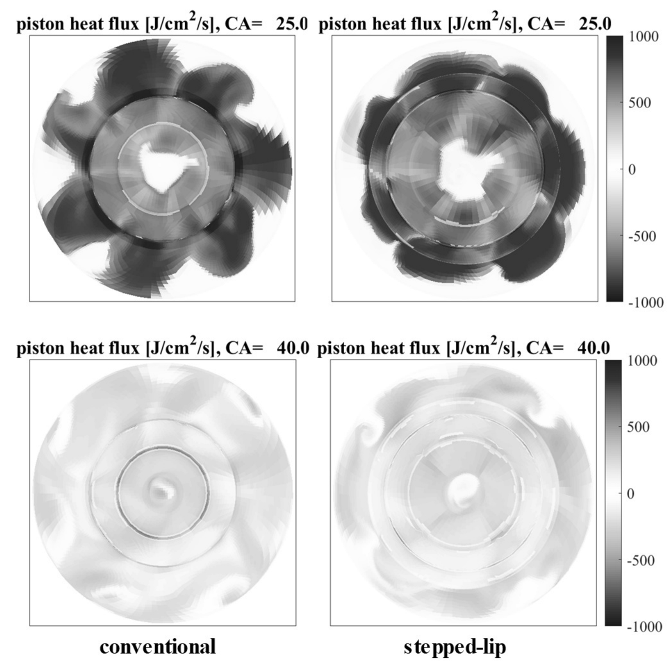

Figure 29. Piston heat flux comparison, SSE07 case.

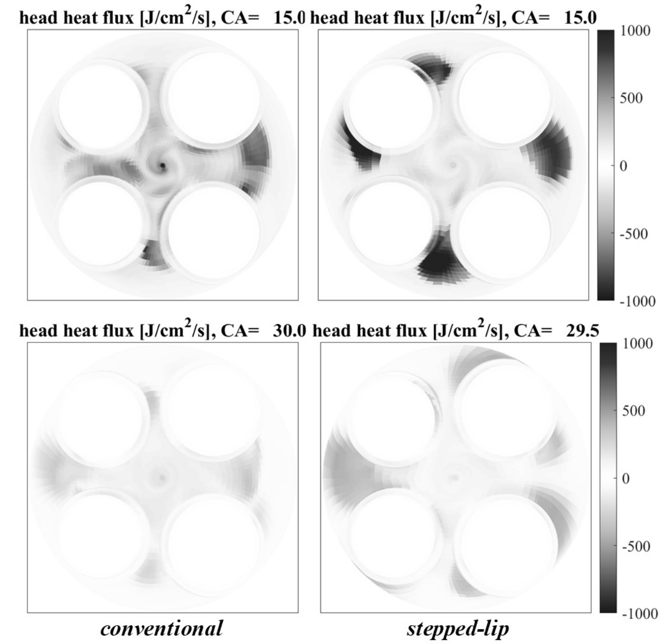

Figure 30. Head heat flux comparison, SSE07 case.

In both cases, heat flux at the piston surface dominates, while liner and head heat fluxes after the start of injection account for between to ~25% and ~35% of the total heat flux, with increasing weight late cycle, when instantaneous heat release due to combustion is low. The heat flux pattern at the piston is unvaried, with clear correlation with heat release timing, and greater heat flux for the conventional piston. Head and liner heat flux patterns instead vary with the injection timing. These results agree fairly well with the medium-load comparison of pistons 1 and 3 in Fridricksson et al. [41].

Piston heat flux. A representation of local heat flux at the piston surface is reported in Figure 29. Both during the injection and late-cycle, local heat flux is defined by the footprint of hot temperature gases above the piston surface. Late cycle, hot gases cover nearly the whole surface, while during injection some areas of the squish volume and the center of the bowl are still uncovered. However, local heat flux coefficients are much higher thanks to higher gas temperature.

The role of piston surface area was analyzed by looking at time integrals of wall heat flux through the piston surface. The conventional bowl geometry has a total piston surface (not including the crevice) of 74.95 cm^2, while the stepped-lip piston geometry has a total surface of 67.23 cm^2, approximately 10.3% smaller. Figures 31 and 32 show that, regardless of injection timing, piston performance is unvaried: both pistons produce nearly identical per-unit-area wall heat fluxes, which suggests that the greater surface area is what causes larger heat flux with the conventional piston.

Head and liner flux. Secondary fluxes vary significantly both with injection timing and with piston shape. Regarding the effect of injection timing, Figures 27 and 28 show that a similar pattern is experienced regardless of piston geometry. With a near-TDC main injection (SSE17), head and liner fluxes are limited by the small squish volume and relatively limited hot gas penetration into the squish toward the liner.

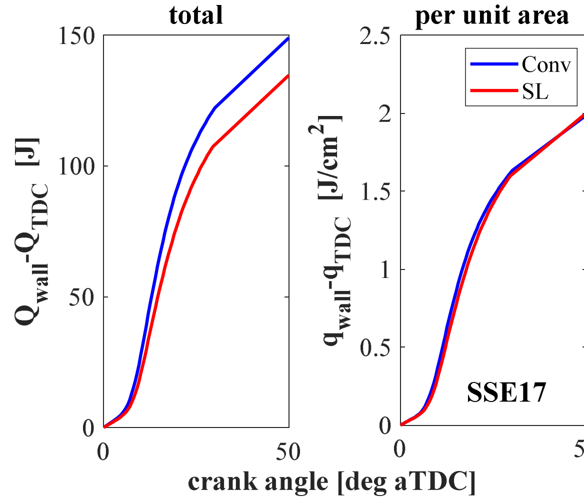

Figure 31. Integral piston heat flux, SSE17 case. (left) total flux; (right) surface-averaged flux.

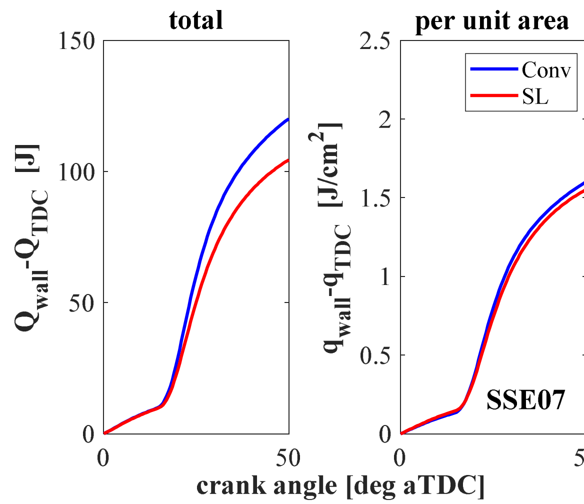

Figure 32. Integral piston heat flux, SSE07 case. (left) total flux; (right) surface-averaged flux.

With a late main injection (SSE07), much more hot gases are being deviated into the squish volume, which leads to higher wall heat transfer. As represented in Figure 30, head heat flux with the stepped-lip geometry is larger than with the conventional bowl when upward flow redirection at the step lip is strong enough to create high-momentum impact against the cylinder head. Overall, this phenomenon still leads to approximately one order of magnitude smaller heat flux than from the piston surface, hence, not too relevant for thermal efficiency. However, it may lead to increased thermal fatigue of the head and valve components.

Concluding remarks

In this study, the effect of piston geometry on combustion behavior in a high-speed, direct injected diesel engine was studied using computational fluid dynamics. The Sandia National Laboratories optical diesel engine, equipped with a stepped-lip piston and a conventional, omega-shaped piston, was simulated, operating a conventional diesel combustion mode with two injection timings, for which extensive experimental validation had been previously achieved.

Following validation of the in-cylinder flow structures, the following analyses were conducted: ignition of the pilot and main injections via tracking of the in-cylinder high-temperature clouds; effects of swirl ratio and injection rate transient; in-cylinder mixing fluxed; wall heat transfer.

The following conclusions were drawn:

- The pilot injection behaves as in a homogeneous reactor: advected, but not significantly mixed by the flow field inside the bowl. Its ignition delay time is mostly affected by the local, turbulent flow features, and not much by bulk transport (swirl).

- Bowl swirl ratio and in-cylinder flow do not affect the pilot IDT, but are critical to capturing the pilot-main jet interaction. This phenomenon affects actual engine operation: the extent to which swirl transports the pilot mixture varies cycle-by-cycle and jet-by-jet. Capturing these effects in a simulation is also necessary to predict correct heat release rates.

- Ignition of the main injection follows different mechanisms: with a conventional bowl, it is driven by stagnation of fuel at the thick piston bowl rim; hence, it is not very sensitive to the relative pilot-main clocking, and only slightly more sensitive to rail pressure. With a stepped-lip bowl, ignition correlates more strongly with the amount of overlap with the hot pilot injected pockets; hence, it is more sensitive to operating parameters such as bowl swirl ratio and rail pressure.

- The stepped-lip piston geometry exhibited better late-cycle mixing behavior, thanks to the lack of a stable vortex structure inside the bowl, caused by smaller bowl volume and by weaker penetration into that area. This explained the better late-cycle soot oxidation behavior observed. Early, injection-driven mixing was instead similar to that of the conventional bowl.

- Wall heat transfer is strongly affected by the piston geometry: with a stepped-lip piston, lower wall heat losses were seen at the piston surface, where a correlation with the piston surface area was observed. Heat transfer at the cylinder head and at the liner could be worse with a stepped-lip piston, as hot gases are more directed towards the head and liner regions and locally higher heat transfer coefficients are produced. However, the latter affect overall heat transfer by never more than 20-30%.

References

[1] J. Styron, B. Baldwin, B. Fulton, D. Ives and R. Subramanian, "Ford 2011 6.7L Power Stroke® Diesel Engine Combustion System Development," in *SAE Technical Paper 2011-01-0415*, Detroit, 2011.

[2] P. C. Miles, B. H. RempelEwert and R. D. Reitz, "Squish-Swirl and Injection-Swirl Interaction in Direct-Injection Diesel Engines," in *ICE2003 6th International Conference on Engines for Automobiles*, Capri, Italy, 2003.

[3] F. Perini, K. Zha, S. Busch, E. Kurtz, R. C. Peterson, A. Warey and R. D. Reitz, "Piston geometry effects in a light-duty, swirl-supported diesel engine: flow structure characterization," *International Journal of Engine Research,* vol. OnlineFirst, 2017.

[4] E. Kurtz and J. Styron, "An Assessment of Two Piston Bowl Concepts in a Medium-Duty Diesel Engine," *SAE International Journal of Engines,* vol. 5, no. 2, pp. 344-352, 2012.

[5] P. C. Miles and O. Andersson, "A review of design considerations for light-duty diesel combustion systems," *International Journal of Engine Research,* vol. 17, no. 1, pp. 6-15, 2016.

[6] D. D. Wickman, H. Yun and R. D. Reitz, "Split-Spray Piston Geometry Optimized for HSDI Diesel Engine Combustion," *SAE Transactions Journal of Engines,* vol. 112, no. 3, pp. 488-507, 2003.

[7] J. G. Dolak, Y. Shi and R. D. Reitz, "A Computational Investigation of Stepped-Bowl Piston Geometry for a Light Duty Engine Operating at Low Load," in *SAE Technical Paper 2010-01-1263*, Detroit, 2010.

[8] D. Yoo, D. Kim, W. Jung, N. Kim and D. Lee, "Optimization of Diesel Combustion System for Reducing PM to Meet Tier4-Final Emission Regulation without Diesel Particulate Filter," in *SAE Technical Paper 2013-01-2538*, Detroit, 2013.

[9] T. Eder, P. Luckert, M. Kemmner and H. Sass, "OM654-Launch of a New Engine Family by Mercedes-Benz," *MTZ Worldwide,* vol. 77, no. 3, pp. 60-67, 2016.

[10] X. Li, Z. Sun, W. Du and R. Wei, "Research and Development of Double Swirl Combustion System for a DI Diesel Engine," *Combustion Science and Technology,* vol. 182, no. 8, pp. 1029-1049, 2010.

[11] S. Busch, K. Zha, E. Kurtz, A. Warey and R. C. Peterson, "Experimental and Numerical Studies of Bowl Geometry Impacts on Thermal Efficiency in a Light-Duty Diesel Engine," in *SAE Technical Paper 2018-01-0228*, 2018.

[12] S. Busch, K. Zha, F. Perini, R. D. Reitz, E. Kurtz, A. Warey and R. Peterson, "Bowl Geometry Effects on Turbulent Flow Structure in a Direct Injection Diesel Engine," in *SAE Technical Paper 2018-01-1794*, Heidelberg, Germany, 2018.

[13] F. Perini and R. D. Reitz, "FRESCO - an object-oriented, parallel platform for internal combustion engine simulations," in *28th International Multidimensional Engine Modeling User's Group Meeting at the SAE Congress*, Detroit, 2018.

[14] F. Perini, S. Busch, K. Zha and R. D. Reitz, "Comparison of Linear, Non-linear and Generalized RNG-based k-epsilon models for turbulent diesel engine flows," in *SAE Technical Paper 2017-01-0561*, Detroit, MI, 2017.

[15] F. Perini and R. D. Reitz, "Improved atomization, collision and sub-grid scale momentum coupling models for transient vaporizing engine sprays," *International Journal of Multiphase Flows,* vol. 79, pp. 107-123, 2016.

[16] "ECN Data Search Page," [Online]. Available: https://ecn.sandia.gov/ecn-data-search/. [Accessed 28 08 2018].

[17] S. Busch, "Light-Duty Diesel Combustion," in *DOE Vehicle Technologies Office and Hydrogen and Fuel Cells Program Annual Merit Review*, Washington, DC, 2017.

[18] F. Perini, E. Galligani and R. D. Reitz, "A study of direct and Krylov iterative solver techniques to approach linear scaling of the integration of Chemical Kinetics with detailed combustion mechanims," *Combustion and Flame,* vol. 161, no. 5, pp. 1180-1195, 2014.

[19] F. Perini, E. Galligani and R. D. Reitz, "An analytical Jacobian approach to sparse reaction kinetics for computationally efficient combustion modelling with large reaction mechanisms," *Energy&Fuels,* vol. 26, no. 8, pp. 4804-4822, 2012.

[20] F. Perini, "High-dimensional, unsupervised cell clustering for computationally efficient engine simulations with detailed combustion chemistry," *Fuel,* vol. 106, pp. 344-356, 2012.

[21] F. Perini, B. Das Adhikary, J.-H. Lim, X. Su, Y. Ra, H. Wang and R. D. Reitz, "Improved Chemical Kinetics Numerics for the Efficient Simulation of Advanced Combustion Strategies," *SAE International Journal of Engines,* vol. 7, no. 1, pp. 243-255, 2014.

[22] K. Radhakrishnan and A. C. Hindmarsh, "Description and use of LSODE, the Livermore Solver for Ordinary Differential Equations," NASA Lewis Research Center, Cleveland, OH, 1993.

[23] Y. Ra and R. D. Reitz, "A combustion model for IC engine combustion simulations with multi-component fuels," *Combustion and Flame,* vol. 158, no. 1, pp. 69-90, 2011.

[24] B.-L. Wang, P. C. Miles, R. D. Reitz and Z. Han, "Assessment of RNG Turbulence Modeling and the Development of a Generalized RNG Closure Model," in *SAE Technical Paper 2011-01-0829*, Detroit, MI, 2011.

[25] R. D. Reitz and F. V. Bracco, "On the Dependence of Spray Angle and Other Spray Parameters on Nozzle Design and Operating Conditions," in *SAE Technical Paper 790494*, 1979.

[26] J. C. Beale and R. D. Reitz, "Modeling Spray Atomization with the Kelvin-Helmholtz/Reyleigh-Taylor Hybrid Model," *Atomization and Sprays,* vol. 19, no. 7, pp. 623-650, 1999.

[27] A. Munnannur and R. D. Reitz, "Comprehensive Collision Model for Multidimensional Engine Spray Computations," *Atomization and Sprays,* vol. 9, no. 6, pp. 597-619, 2009.

[28] D. J. Torres, P. J. O'Rourke and M. F. Trujillo, "A Discrete Multicomponent Fuel Model," *Atomization and Sprays,* vol. 13, no. 2&3, p. 42, 2003.

[29] F. Perini, A. B. Dempsey, R. D. Reitz, D. Sahoo, B. Petersen and P. C. Miles, "A Computational Investigation of the Effects of Swirl Ratio and Injection Pressure on Mixture Preparation and Wall Heat Transfer in a Light-Duty Diesel Engine," in *SAE Technical Paper 2013-01-1105*, Detroit, MI, 2013.

[30] S. Busch and P. C. Miles, "Parametric Study of Injection Rates With Solenoid Injectors in an Injection Quantity and Rate Measuring Device," in *ASME Paper No. ICEF2014-5583*, Columbus, Indiana, USA, 2015.

[31] "Small-Bore Diesel Engine," Sandia Mational Laboratories, 11 8 2017. [Online]. Available: https://ecn.sandia.gov/engines/engine-facilities/small-bore-diesel-engine/. [Accessed 2018].

[32] F. Perini, R. D. Reitz and P. C. Miles, "A comprehensive modeling study of in-cylinder fluid flows in a high-swirl, light-duty optical diesel engine," *Computers and Fluids,* vol. 105, pp. 113-124, 2014.

[33] F. Perini, S. Busch, E. Kurtz, A. Warey, R. C. Peterson and R. D. Reitz, "Limitations of Sector Mesh Geometry and Initial Conditions to Model Flow and Mixture Formation in Direct-Injection Diesel Engines," in *SAE Techical Paper 2019-01-0204*, Detroit, 2019.

[34] K. Zha, S. Busch, A. Warey, R. C. Peterson and E. Kurtz, "A Study of Piston Geometry Effects on Late-Stage Combustion in a Light-Duty Optical Diesel Engine Using Combustion Image Velocimetry," in *SAE Technical Paper 2018-01-0230*, 2018.

[35] R. P. Hessel, R. D. Reitz, M. P. B. Musculus, J. O'Connor and D. Flowers, "A CFD Study of Post Injection Influences on Soot," *SAE International Journal of Engines,* vol. 7, no. 2, pp. 694-713, 2014.

[36] C. J. Mueller, "The Quantification of Mixture Stoichiometry When Fuel Molecules Contain Oxidizer

Elements or Oxidizer Molecules Contain Fuel Elements," in *SAE Technical Paper 2005-01-3705*, Detroit, 2005.

[37] F. Perini, K. Hiraoka, K. Nomura, A. Yuuki, Y. Oda, C. J. Rutland and R. D. Reitz, "An Efficient Level-Set Flame Propagation Model for Hybrid Unstructured Grids using the G-Equation," *SAE International Journal of Engines,* vol. 9, no. 3, pp. 1409-1424, 2016.

[38] F. Perini, S. Busch and R. D. Reitz, "A phenomenological rate of injection model for predicting fuel injection with application to mixture formation in light-duty diesel engines," *Proc. IMechE Part D: Journal of Automobile Engineering,* vol. 0, no. 0, p. 29, submitted.

[39] G. Zhu, K. Pattabiraman, F. Perini and C. J. Rutland, "Modeling Ignition and COmbustion in Spark-Ignition Engines Based on Swept-Volume Method," in *SAE Technical Paper 2018-01-0188*, Detroit, 2018.

[40] Z. Han and R. D. Reitz, "A temperature wall function formulation for variable-density turbulent flows with application to engine convective heat transfer modeling," *International Journal of Heat and Mass Transfer,* vol. 40, no. 3, pp. 613-625, 1997.

[41] H. S. Fridriksson, M. Tuner, O. Andersson, B. Sunden, H. Persson and M. Ljungqvist, "Effect of Piston Bowl Shape and Swirl Ratio on Engine Heat Transfer in a Light-Duty Diesel Engine," in *SAE Technical Paper 2014-01-1141*, Detroit, 2014.

[42] F. Perini, K. Zha, S. Busch, P. C. Miles and R. D. Reitz, "Principal Component Analysis and Study of Port-Induced Swirl Structures in a Light-Duty Optical Diesel Engine," in *SAE Technical Paper 2015-01-1696*, Detroit, MI, 2015.

Contact Information

Federico Perini
Federico.Perini@w-erc.com

Acknowledgments

This work was performed under Sandia Subcontract 1890589, 1, sponsored by the United States Department of Energy, Office of Vehicle Technologies, with program managers Gupreet Singh and Michael Weismiller.

Sandia National Laboratories is a multi-mission laboratory managed and operated by National Technology and Engineering Solutions of Sandia, LLC., a wholly owned subsidiary of Honeywell International, Inc., for the U.S. Department of Energy’s National Nuclear Security Administration under contract DE-NA-0003525. The views expressed in the article do not necessarily represent the views of the U.S. Department of Energy or the United States Government.

The authors also gratefully acknowledge support and computational resources for this work at the Cineca super-computing center by the EC Research Innovation Action under the H2020 Program, through HPC-EUROPA3 grant HPC17FFPU6.